Tropical Cyclones Downscaled from Simulations of the Last Glacial Maximum

QUINTON A. LAWTON,[a,b] ROBERT L. KORTY,[a] AND RYAN A. ZAMORA[a,c]

[a] *Texas A&M University, College Station, Texas*

(Manuscript received 1 June 2020, in final form 14 October 2020)

ABSTRACT: The tracks, intensities, and other properties of tropical cyclones downscaled from three models' simulations of the Last Glacial Maximum (LGM) are analyzed and compared to those of storms downscaled from simulations of the present climate. Globally, the mean maximum intensity of storms generated from each model is lower at LGM, as is the fraction of all storms that reach intensities of category 4 or higher on the Saffir–Simpson hurricane wind scale. The median day of the storm season shifts earlier by an average of one week in all three models in both hemispheres. Two of the three models' LGM simulations feature a reduction in storm count and global power dissipation index compared to the current climate, but a third shows no significant difference between the two climates. Although each model is forced by the same global changes, differences in the way sea surface temperatures and other large-scale environmental conditions respond in the North Atlantic impart significant differences in the climatology at LGM between models. Our results from the cold LGM provide a novel opportunity to assess how tropical cyclones respond to climate changes.

KEYWORDS: Tropical cyclones; Climate change; Paleoclimate; Climate models

1. Introduction

Tropical cyclones (TCs) are warm-core, convective storms that acquire energy from ocean-to-atmosphere fluxes of heat and moisture, and the mechanisms that drive them can operate at any latitude and in any climate in which the conditions that support them exist. The large-scale environment in which these storms are embedded must be conducive for them to form and intensify. Low vertical wind shear, elevated midlevel humidity (so that any air entrained at midlevels is less severely dry), and thermal environmental soundings permitting deep convection through the troposphere have all been shown to be necessary conditions for these systems to exist and thrive (DeMaria 1996; Camargo et al. 2007; Tang and Emanuel 2010; Nolan 2011). Importantly, the existence of these storms is not predicated on any particular sea surface temperature (SST), as the isotherms encircling areas with favorable thermodynamic conditions vary with climate (Emanuel 1987; Royer et al. 1998; Korty et al. 2012a,b, 2017; Koh and Brierley 2015; Yan et al. 2015, 2016, 2019) and depend on how climate changes (Emanuel and Sobel 2013). A remarkable consequence of this is that even though tropical cyclones rarely form over water colder than 26.5°C in today's climate (Palmen 1948; Gray 1968), environmental conditions at the height of the Last Glacial Maximum (LGM) 21 000 years ago also supported TCs (Korty et al. 2012a; Koh and Brierley 2015), even though SST was colder throughout the tropics (Annan and Hargreaves 2013). While there have been scattered attempts to simulate TCs under LGM conditions (Hobgood and Cerveny 1988; Yoo et al. 2016), in this paper we present the first global set of tropical cyclones downscaled from climate conditions at the LGM.

Analyzing aspects of TCs' climatology using past climate simulations (Korty et al. 2008, 2012a,b, 2017; Fedorov et al. 2010; Koh and Brierley 2015; Yan et al. 2015, 2016, 2019; Yoo et al. 2016; Yan and Zhang 2017; Pausata et al. 2017) offers a useful complement to the extraordinary progress made over the past 15 years to understand how TCs respond to contemporary climate change (e.g., Emanuel 2005; Webster et al. 2005; Emanuel 2013; Kossin et al. 2014; Walsh et al. 2016; Sobel et al. 2016; Camargo and Wing 2016; Kossin 2018; Knutson et al. 2019, 2020; Lee et al. 2020). The climates of the geologic past are quite varied and can be further removed from present conditions than are the projected anthropogenic changes underway this century. The forces creating the different surface conditions are also more varied—for example, not only changes in greenhouse gas concentrations, but also large changes in surface characteristics, continental positions (in deep geologic time), and variations in Earth's orbit that alter the seasonal cycle of incoming solar radiation. Exploring this variety is important because even if two distinct external forces yield similar changes in surface temperatures, atmospheric circulations and thermal stratifications aloft may respond in very different ways to them (e.g., Emanuel and Sobel 2013; Zamora et al. 2016; Yan et al. 2020). Thus, while there are presently no geologic proxy records of storms from as long ago as the LGM, simulations of this period offer a unique opportunity to explore how TCs respond to glacial climates as well as add an important contrast to the TC-climate research focusing on the response of TCs to warming. Also, although the great majority of proxy storm records span only the last two millennia, emerging techniques using offshore cores and marine caverns have recorded evidence of earlier storms deposited during the early Holocene and Younger Dryas (Toomey et al. 2013, 2017; van Hengstum et al. 2020), raising at least some hope that records of older storms may become possible.

Emanuel (2006) developed a method to downscale TCs using a parent global model's thermodynamic conditions and

[b] Current affiliation: Rosenstiel School of Marine and Atmospheric Science, University of Miami, Miami, Florida.

[c] Current affiliation: Johns Hopkins University, Baltimore, Maryland.

Corresponding author: Quinton A. Lawton, quinton.lawton@rsmas.miami.edu

DOI: 10.1175/JCLI-D-20-0409.1

tropospheric winds to simulate the conditions along the tracks that TCs would be steered. The method, which is reviewed in greater detail in section 2, has successfully reproduced properties of the modern TC climatology when driven by reanalyses or by simulations of present-day conditions, and it has also been employed to explore the behavior of TCs under anthropogenic warming and in paleoclimates (e.g., Emanuel et al. 2008; Emanuel 2013; Fedorov et al. 2010; Pausata et al. 2017; Korty et al. 2017). Here we report results of this downscaling technique applied to the glacial climates at the LGM: we analyze storms statistically downscaled from three simulations of the climate 21 000 years ago, when large ice sheets covered much of North America and Europe. Surface temperatures were colder globally, and both model simulations and proxy reconstructions of SSTs show that those in the tropics were likely 1°–4°C colder than during the present day (Annan and Hargreaves 2013). Coupled with the fact that much of the Northern Hemisphere's polar latitudes were covered in ice and had substantially lower annual mean surface temperatures, meridional temperature gradients were also larger in subtropical and middle latitudes than today. The LGM climate has been simulated by several generations of climate models, and phase 3 of the Paleoclimate Model Intercomparison Project (PMIP3) included LGM simulations from several established modeling groups. Each model was forced with the same set of prescribed conditions (e.g., CO_2 was 185 ppm and large ice sheets covered much of North America and Europe). However, substantial intermodel variability has been documented in the storms directly simulated by climate models using present-day conditions (Camargo 2013), and so we consider how TCs respond in LGM simulations of three different models here. Our primary goals for this paper are twofold: 1) to analyze how the colder environment at the LGM affects the climatology of downscaled TCs, and 2) to show that models forced with the same conditions can yield quite different responses to TCs, especially regionally.

We review the models and downscaling methodology in the next section and present the climatology of LGM TCs in section 3. Because some properties of the TC climatology at LGM differ among the three models examined, in section 4 we examine some underlying differences between the models' twentieth-century simulations (used as control cases) and observational data to help understand the sources of variability in individual model responses. We focus on some intermodel variability by basin in section 5, and we compare our findings to the current understanding of TCs and climate in the conclusions.

2. Data and methods

We analyze TCs downscaled from the historical runs and LGM simulations of three models contributed to PMIP3: The Community Climate System Model version 4.0 (CCSM4; henceforth simply CCSM), the Meteorological Research Institute CGCM Version 3 (MRI-CGCM3; henceforth MRI), and the Max Planck Institute for Meteorology Earth System Model (MPI-ESM; henceforth MPI). The control cases are downscaled from historical simulations of each model using the period 1980–2005 (the late twentieth and early twenty-first century; henceforth C20), and glacial cases are generated from 30 years of each model's LGM simulation (equilibrium simulations of climate conditions found 21 000 years ago). Because the downscaling method requires upper and lower tropospheric winds at daily frequencies to capture the variability in shear and steering flows, the methodology can be applied only to the limited number of years for which high-frequency data from the LGM experiments was archived. These glacial simulations are forced with large ice sheets [blended from three reconstructions; see Abe-Ouchi et al. (2015) for details], lower CO_2 (185 ppm), lower methane (CH_4; 350 ppb), contain no chlorofluorocarbons (CFCs), and use the same ozone (O_3) levels prescribed in the preindustrial era control simulations (Braconnot et al. 2012; Brady et al. 2013). Forced with these radically different conditions, models produce significantly colder surface temperatures that have broad qualitative agreements with proxies of the period. However, there are significant regional differences among the simulated responses: notable among these are whether the Southern Hemisphere midlatitude jet shifts equatorward or poleward at LGM and the sign of precipitation anomalies in the western Pacific and Maritime Continent (Harrison et al. 2014, 2015).

a. Review of downscaling methodology

Emanuel (2006) and Emanuel et al. (2008) introduced a novel method to statistically downscale TCs from the large-scale properties of parent global climate models, which we apply here to the LGM and C20 simulations described above. A large number [$O(10^6)$] of weak initial vortices are randomly distributed over all ocean basins at all times of the year, and they are advected by the model's deep layer tropospheric flow, defined by the 250- and 850-hPa level winds (and corrected for "beta drift"), to determine their future paths. The Coupled Hurricane Intensity Prediction Scheme (CHIPS), an axisymmetric model described in Emanuel (1995) and Emanuel et al. (2004), is called to simulate the evolution of each initial vortex. Naturally, the vast majority of these initial vortices were placed in environments with hostile thermodynamic and other large-scale conditions, and thus most fail to develop into a TC. Those that do intensify are followed along their track, along which they face evolving large-scale conditions, until landfall or hostile environmental conditions dictate their demise. This process is continued until a preselected number of events is generated. The total number of seed vortices required to reach this threshold is used to define a success rate and calibrate the climatological frequency of TC genesis to an average of 80 per year in C20, which is chosen to match the observed global frequency of the historical record (Anthes 1982; Frank and Young 2007). This calibrated success rate is then used to find the frequency of storms in the LGM. For example, if an LGM simulation required twice as many seeds to generate the same number of events, its reported annual frequency of TCs would be half that of the control experiments.

Differences in climatological properties between storm sets from the two different climates are assessed for statistical significance using Welch's unequal variance t test. A change is considered significant at a 95% confidence level, with the null hypothesis being equal means in the two climate states. Global attributes such as annual storm count or mean intensity are tabulated for each of the 30 LGM years and 26 years in C20 and then each climate's mean values are compared using Welch's

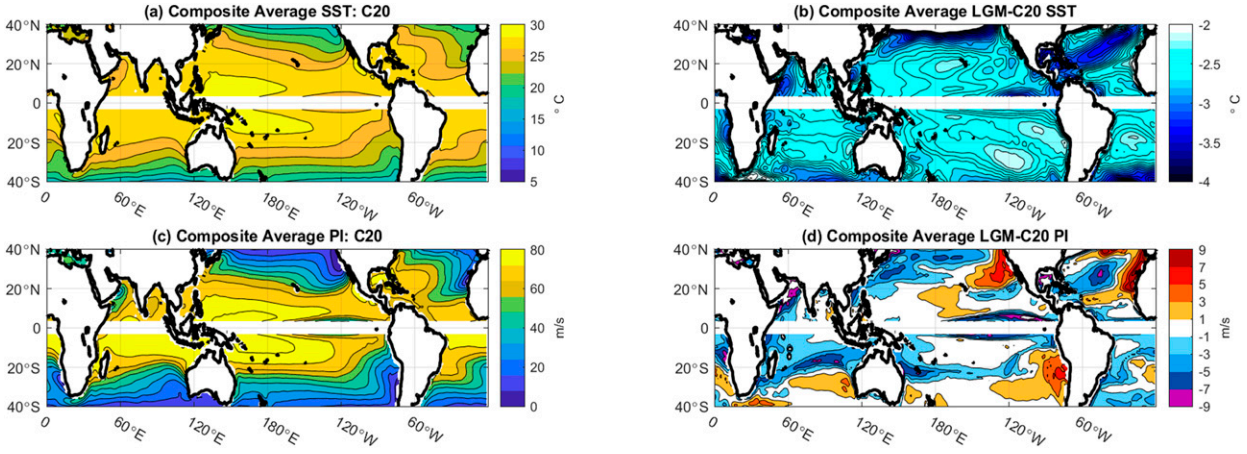

FIG. 1. (a) Composite storm season average (July–October in Northern Hemisphere, January–April in Southern Hemisphere) SST from the C20 ensemble, and (b) composite storm season average SST differences between LGM and C20. (c),(d) As in (a) and (b), but for potential intensity. The grid points adjacent to and at the equator are intentionally kept blank to highlight that each hemisphere is averaged over a distinct range of months.

test. For spatial fields such as power dissipation, significance is evaluated using the same method but is assessed locally at each grid point.

b. *Potential intensity and SST at LGM*

To help analyze why there are differences between the LGM and C20 climatology of downscaled TCs, we consider how several large-scale environmental factors change in the colder glacial atmosphere. While sea surface temperatures (SSTs) are universally colder at LGM (Figs. 1a,b), with most regions of the tropics ~2.5°C colder during the late summer and autumn storm seasons, the effect of this surface cooling on TCs is best understood in the context of potential intensity (Emanuel 1987; Royer et al. 1998; Emanuel and Sobel 2013; Korty et al. 2017). Surface temperatures change in conjunction with vertical profiles of temperature, which to first order are set and maintained by moist convective processes in the deep tropics (Xu and Emanuel 1989; Korty and Emanuel 2007; Zamora et al. 2016). Even though the surface was colder in the LGM, so too was the troposphere above it, and the surface enthalpy fluxes on which TCs depend can still deliver a robust transfer of heat from the ocean to atmosphere in a glacial climate.

To quantify these effects, we calculate potential intensity (PI), which gives the maximum possible TC intensity set by the thermodynamics, following the algorithm developed by Bister and Emanuel (2002):

$$\mathrm{PI} = \sqrt{\frac{C_k}{C_d}\frac{\mathrm{SST}}{T_o}(\mathrm{CAPE}^* - \mathrm{CAPE}^b)}. \qquad (1)$$

PI depends on the ratio of the exchange coefficients for enthalpy C_k and drag C_d from bulk aerodynamic formulas and on the ratio of SST to the temperature at the level of convective outflow T_o, which must be determined from the vertical sounding of temperature and moisture. CAPE is the vertical integral of parcel buoyancy, which depends on the parcel's temperature, humidity, and pressure. CAPE* in (1) is the value of CAPE an air parcel would have if it were saturated at the SST and lifted from the radius of maximum winds; CAPE^b is the value of CAPE for a parcel lifted from the ambient boundary layer whose pressure was first reduced isothermally to that of the radius of maximum winds [see Bister and Emanuel (2002) for additional details]. PI in (1) gives the maximum possible near-surface wind speed (measured as the 10-m wind speed in units of $\mathrm{m\,s^{-1}}$) for a given thermodynamic sounding.

We build composites for each climate by interpolating each model's fields to a common spatial grid and then averaging the three models' values at each grid point. Figure 1c shows the three-model composite storm season average PI (defined as July–October in the Northern Hemisphere, and as January–April in the Southern Hemisphere) for C20. Although PI is high where SST is high, there is not a direct relationship between them. Rather, PI is high where the vertical soundings permit deep convection (common throughout the deep tropics), and values drop abruptly at the subtropical margin where trade inversions act as a cap on convection (see Korty et al. 2012a). Figure 1d shows the composite difference between LGM and C20 values of PI during each hemisphere's storm season. Despite the fact that SSTs are 2°–3°C colder throughout the tropics, PI shows little change between the two climates in several basins, and it remains large enough to support TCs in the tropics of all three models at LGM. There is little difference in the western North Pacific and in the tropical eastern North Pacific, while it is actually higher at LGM in much of the central Pacific. Composite values are lower at LGM in much of the Atlantic and southern Indian Oceans. Vecchi and Soden (2007) showed regions where tropical temperatures are warmer than the tropical mean tend to have the highest PI, while areas with local temperatures

TABLE 1. Large-scale properties of each model's simulations and the climatology of TCs downscaled from them: tropical (30°S–30°N) and global annual mean SST (°C), and annually integrated power dissipation index (PDI; 10^{12} m^3 s^{-2}) for C20 and LGM simulations of each model. SST averages exclude regions covered by sea ice. Changes in PDI that are not statistically significant (at a 95% confidence threshold) are shown in italics.

	CCSM		MPI		MRI	
	C20	LGM	C20	LGM	C20	LGM
Tropical mean SST (°C)	26.5	23.6	25.7	23.3	25.8	23.2
Global mean SST (°C)	20.7	18.9	19.1	17.8	20.1	18.4
Global PDI (10^{12} m^3 s^{-2})	2.2	1.73 (−21.6%)	1.9	1.4 (−26.7%)	3.2	*3.2 (0%)*

below the tropical mean tend to have lower PI. Korty et al. (2012a) showed similar behavior exists in LGM simulations and noted that changes in PI were strongly tied to the difference of SST between climates. Local changes in thermodynamic favorability are not solely a product of shifts in SST, but rather how SSTs change relative to that of the tropical mean.

c. *Vertical wind shear and combined metrics*

Vertical wind shear can play a detrimental role in the life of a TC by mixing midlevel environmental air (which, being subsaturated, is relatively dry) into the core of storm; we calculate this deep layer shear as the magnitude of the vector difference of the 250- and 850-hPa level winds.[1] Tropical cyclones also benefit from locally high levels of humidity in the middle troposphere; this can hasten the incubation period during which surface fluxes must supply sufficient moisture to saturate the column, and it also guards against the detrimental effects of ventilating environmental air into the core of a storm in the presence of vertical shear (Tang and Emanuel 2010, 2012). An early genesis index proposed using relative humidity as a factor to capture these areas (Emanuel and Nolan 2004), but subsequent work used other formulations that depend on the saturation deficit of the middle troposphere (Emanuel et al. 2008; Tippett et al. 2011; Korty et al. 2017). The latter is strongly temperature dependent (if relative humidity changes are small), as warmer temperatures require exponentially higher amounts of moisture to reach saturation in a column. In the modern climate, both formulations can adequately capture the spatial and temporal structure of genesis locations, but they can point in diametrically opposite directions in climate change experiments (e.g., Lee et al. 2020). Alternatively, Bruyère et al. (2012) argued that potential intensity and vertical shear were sufficient for defining a genesis index based on observations from the North Atlantic. They defined a cyclone genesis index (CGI):

$$\mathrm{CGI} = \left(\frac{\mathrm{PI}}{70}\right)^3 (1 + 0.1V_{\mathrm{sh}})^{-2}, \tag{2}$$

where V_{sh} is the deep layer shear, and PI is defined as in (1), and both velocities are in units of meters per second. We will show that these two factors can explain many of the principal changes and regional differences in the simulations examined here. Furthermore, we found that changes in CGI were qualitatively aligned with changes in PDI despite neglecting the humidity factor.[2] We choose (2) as a simple summary metric for their combined effects of PI and shear (in our case, using a 250–850-hPa wind shear). We assess statistical significance for changes in these environmental metrics in the same manner as we do for spatial changes in the TC climatology: using Welch's t test at each grid point to compare the mean values of environmental parameters between the two climate states for each model.

3. Global properties of downscaled TCs at LGM

The TCs downscaled from LGM and C20 (control case) simulations sample from the environmental conditions of two very different climates, as summarized in Table 1. Although identical ice sheets are prescribed in each model over land, the sea ice coverage is simulated by each model individually and varies between them. Equatorward of 30° latitude, annually averaged tropical mean SSTs are 2.4°–2.9°C colder at LGM than in the C20 simulations (cf. Fig. 1b, which shows the composite SST differences during the late summer to fall storms for each hemisphere). As discussed earlier, TCs are possible in these colder climates because the potential intensity, which depends on the relationship between local SST and the atmosphere's temperature profile above it, remains high. Korty et al. (2012a) showed that high PI was most often found in places with SST > 24°C in LGM simulations.

Figure 2 shows a random selection of downscaled TC genesis points (top two panels) and tracks of high-intensity storms (bottom two panels) drawn from the ensembles of C20 and LGM simulations. Although the number of genesis points and tracks pulled for the LGM climate is adjusted to account for changes in frequency with climate (discussed below), the panels show profound similarities: TCs could form in regions at

[1] We choose to use winds from the 250-hPa level because data from that level are used by the downscaling method. Although their magnitudes differ, the vertical shear computed over the 850–250-hPa layer is highly correlated with other metrics of deep layer wind shear, such as the commonly used 850–200-hPa layer shear.

[2] Although midlevel humidity plays an important role in TC ventilation (Tang and Emanuel 2012), we note two opposing trends in LGM simulations: because they are colder, the saturation deficit would be smaller if relative humidity were constant, but the actual midlevel relative humidity is lower in LGM simulations across almost all of the tropics.

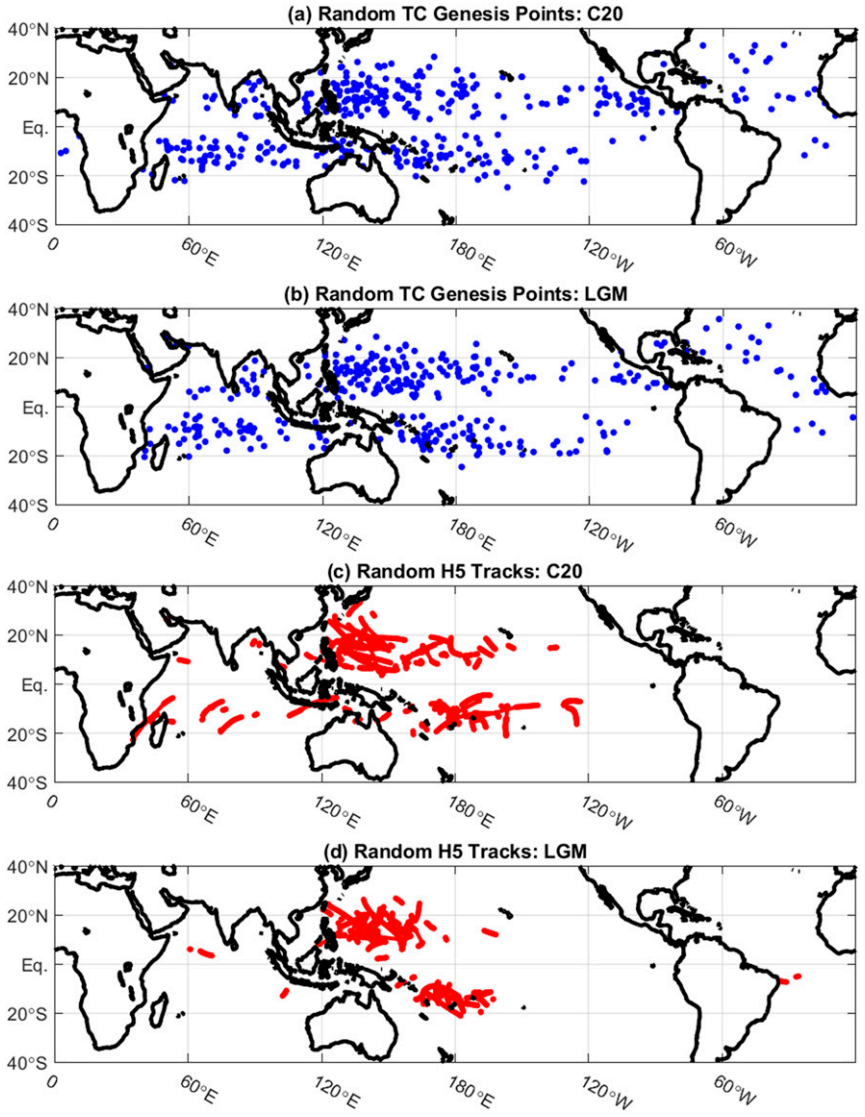

FIG. 2. Randomly selected genesis points, pulled from downscaled data from all three models, are shown for (a) the C20 climate state and (b) at the LGM. In total 400 random points are plotted for C20 while 360 (90% of C20) points are plotted for LGM. This ratio is equivalent to the average difference in total annual count between the LGM and C20 simulations. Randomly selected tracks for TCs when they are at or above H5 strength, also pulled from all three models, are shown (c) for the twentieth-century climate state and (d) at the LGM. Here, 100 random tracks are plotted for C20 and 77 (77% of C20) for LGM. This ratio is equivalent to the average difference in the number of H5 systems between the LGM and C20 simulations.

LGM similar to where they form in C20, and although the frequency becomes less common, storms can still achieve very high intensities at LGM.

a. Annual frequency and intensity distributions

Table 2 shows the number of downscaled TCs, binned by their lifetime maximum intensity, that were generated from each model's LGM and C20 simulations. All numbers have been calibrated to an average total of 80 storms per year in each model's C20 simulation as discussed in the last section.

Two of the models (CCSM and MPI) yield fewer total cases at LGM than C20, but MRI produces about the same number (the small increase is statistically insignificant). CCSM and MPI both yield significantly fewer intense hurricanes (category 4 or 5 on the Saffir–Simpson hurricane wind scale; hereafter, H4 and H5, respectively) at LGM than in C20, but the declines in these categories in MRI are insignificant. The response of weaker hurricanes (H1–H3) is more varied across the models. Declines in the number of events are insignificant for some of these categories in CCSM and MPI, but there is a higher

TABLE 2. Annual frequency of downscaled TCs by intensity category and median genesis day by hemisphere. Numbers are rounded to one decimal place. Annual frequency is shown for both total storms and by category using the Saffir–Simpson hurricane wind scale; LGM counts in italics are not different from C20 values by a statistically significant amount (95% confidence thresholds). The median Julian day of each hemisphere's storm season is shown for both C20 and LGM for each model.

	CCSM		MPI		MRI	
	C20	LGM	C20	LGM	C20	LGM
Annual frequency of all TCs	80.0	64.9	80.0	68.2	80.0	*83.0*
Tropical storms	37.1	30.0	38.1	32.9	29.7	*30.0*
H1	15.6	13.8	17.6	*16.7*	14.7	16.7
H2	6.7	*5.8*	6.4	*6.9*	7.2	8.1
H3	6.9	5.7	7.1	5.4	7.7	9.0
H4	7.7	5.4	6.6	4.3	9.7	*9.1*
H5	5.9	4.2	4.3	2.0	11.0	*10.1*
Median Julian day of genesis (Northern Hemisphere)	247	239	235	225	232	228
Median Julian day of genesis (Southern Hemisphere)	62	56	49	42	55	50

number of events in this intensity range in MRI, which drives the total number of events in this model's LGM simulation higher. Nevertheless, a smaller fraction of each event set reaches H4 intensity or higher in each model's LGM simulation compared to its C20 simulation; the fraction of all storms generated that become H4 or H5 in LGM declines between 2.2% and 4.4% in each of the three models.[3] This is broadly consistent with results from global warming studies that have shown increases in the fraction of storms that reach high intensity categories in warmer climates (Emanuel et al. 2008; Emanuel 2013; Fedorov et al. 2010; Walsh et al. 2016; Camargo and Wing 2016; Sobel et al. 2016; Korty et al. 2017). Our results are also consistent with the explicit simulation of LGM storms in the western North Pacific by Yoo et al. (2016), who also found their average intensity lower.

Given the declines seen in the intensity distribution, CCSM and MPI produce a statistically significant decline in global sum of power dissipation at LGM relative to the C20 control, though the MRI shows no statistically significant change (Table 1). The power dissipation index (PDI) is a combined metric of storm activity that sums the cube of the peak wind speed at each 6-hourly interval over the life of every storm:

$$\text{PDI} = \int V^3 \, dt. \tag{3}$$

Thus, PDI is most strongly influenced by the frequency and duration of the highest intensity events. This decline in the colder LGM for CCSM and MPI is consistent with the behavior seen in simulations of warmer climates, in which PDI increases with warming (e.g., Emanuel 2013; Sobel et al. 2016; Korty et al. 2017). Sources of the intermodel variability will be explored in greater detail in sections 4 and 5.

b. *Spatial distributions of genesis, tracks, and power dissipation*

Figure 3 shows that the regions that spawn TCs are similar between the two climates, but genesis frequency declines in all major TC formation regions at LGM. The C20 patterns of genesis density are qualitatively similar to those of the historical record, though all three models overestimate the relative frequency of Southern Hemisphere storms, where downscaled activity at low latitudes is higher than observed. The declines in LGM genesis seen in CCSM and MPI occur in each of the main basins, highlighted by the reduced spatial extent of the 0.0375 storms per latitude degree squared genesis density line (cf. Figs. 3c,d).[4] Conversely, MRI showed an increase in LGM frequency in the eastern North Pacific, North Atlantic, and South Pacific.

Figure 4 shows the track and power dissipation densities for C20 and LGM. Events downscaled from C20 reproduce several aspects of the observed climatology: the western North Pacific is the most active basin, and Southern Hemisphere tracks are largely confined to the Indian Ocean and southwest Pacific. In LGM, power dissipation density decreases precipitously in subtropical and middle latitudes, and the composite LGM PDI also drops in all tropical basins that produce TCs. Track densities similarly decline, although there are small increases in the subtropical north central Pacific near and poleward of a region in which potential intensity was locally higher at LGM than in the C20 control (Fig. 1d). Conditions in C20 appear to support

[3] Other sensible thresholds used to define intense events show qualitatively similar declines in the fraction of total events. The fraction of storms that reach H3 intensity or higher ("major hurricanes") is also lower in each model's LGM simulation, but the declines in the three models vary by a wider range between 1.6% and 5.2%. The fraction of storms that reach H5 intensity at LGM declines between 0.9% and 2.4% in the three models.

[4] The 0.0375 contour line was selected to outline regions of significant TC activity, which is not sensitive to using slightly higher or lower values.

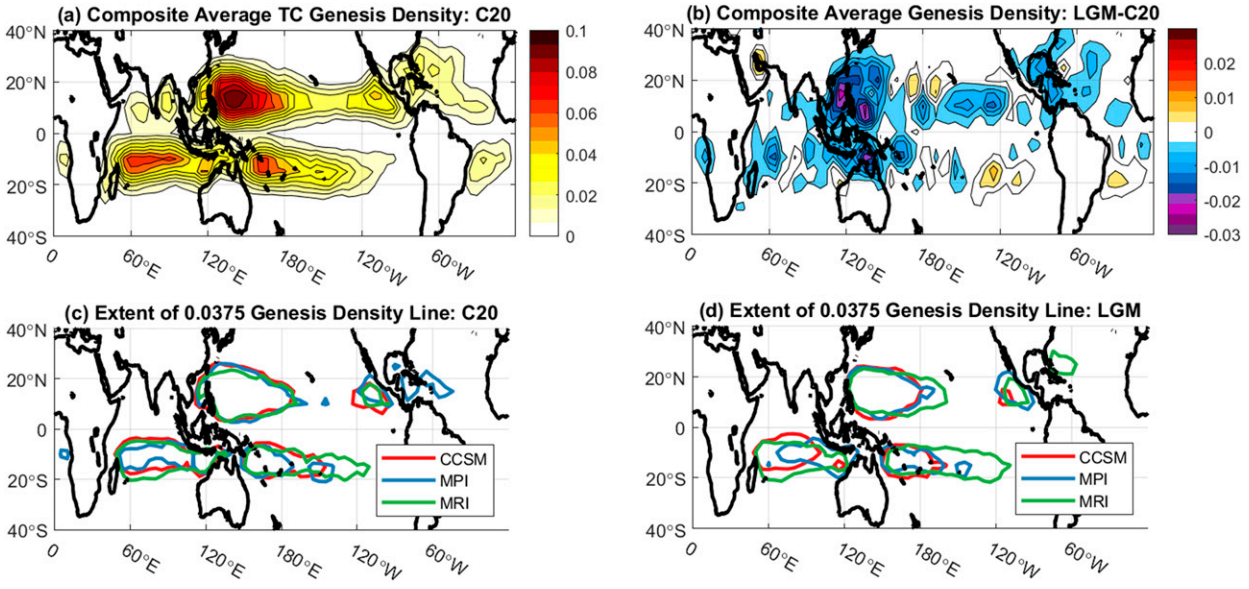

FIG. 3. (a) Composite C20 genesis density in units of number of storms per year per degree of latitude squared; (b) difference in composite genesis density between LGM and C20. (c) Contours of the 0.0375 storms per year per degree of latitude squared threshold for each of the three individual C20 simulations. (d) As in (c), but for LGM. It should be noted that genesis density is originally calculated for $5° \times 5°$ grid boxes, some of which include both ocean and land in their domain. A byproduct of this is that genesis density contours in (a) and (b) occasionally appear to extend over land. This is reflective of genesis events occurring very close to the shoreline, not genesis occurring over land.

TCs in the South Atlantic more readily than is observed in nature.

Figure 5 compares the annual frequency of downscaled TC activity, separated by ocean basin. The overwhelming majority of downscaled TCs in the Northern Hemisphere occur in the western North Pacific, as in the modern era. The overrepresentation of Southern Hemispheric TCs in the composite analysis appears to be driven largely by MRI; it was the only model for which there was consistent downscaled TC activity in the southeastern Pacific. Nevertheless, changes in the annual frequency of Southern Hemisphere TCs across MRI's two climate states were quite small. Distinct intermodel variability is evident in the northern Atlantic, with MRI showing an increase in LGM TC count relative to that of its C20 simulation, in direct contrast to CCSM and MPI. MRI also deviates from these other two models by depicting only a minimal reduction in western Pacific frequency at LGM relative to C20. Southern Hemisphere intermodel variability is large, and prior work has documented intermodel differences in how large-scale circulation shifts at LGM here (Harrison et al. 2015).

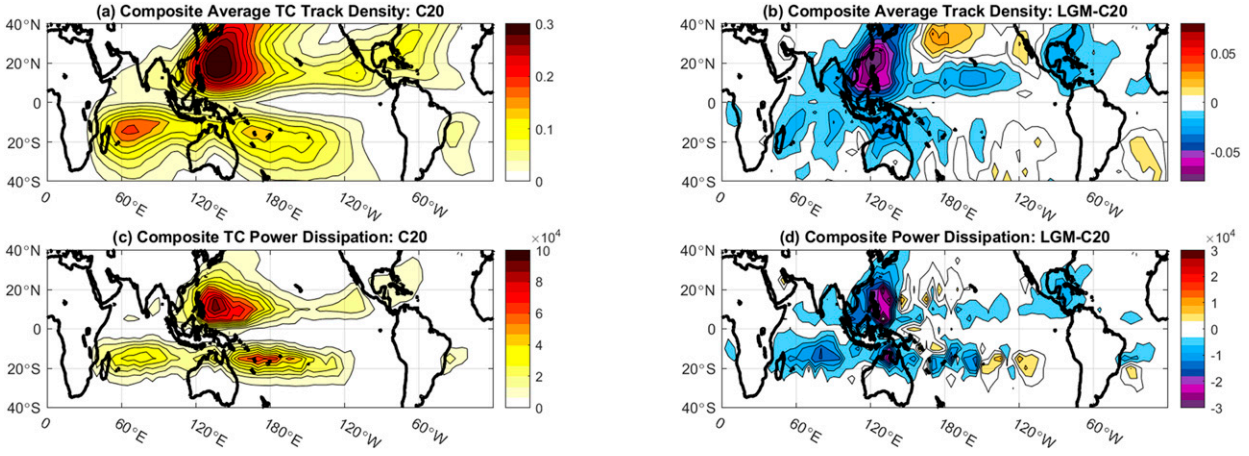

FIG. 4. (a) As in Fig. 3a, but for track density; (b) as in Fig. 3b, but for differences in track density. (c),(d) As in (a) and (b) but for composite power dissipation index.

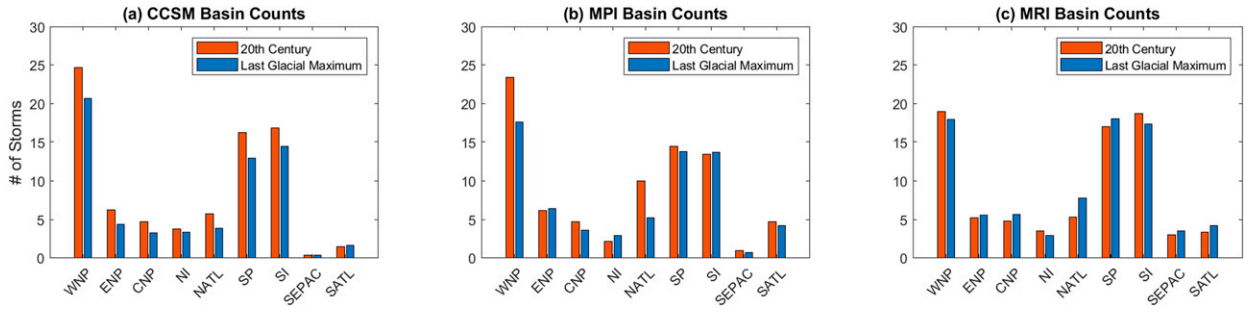

FIG. 5. Annual frequency of downscaled TCs from the (a) CCSM, (b) MPI, and (c) MRI simulations of twentieth-century and LGM climate separated by basin. Included regions are the western North Pacific (WNP), eastern North Pacific (ENP), central North Pacific (CNP), North Indian (NI), North Atlantic (NATL), South Indian (SI), South Pacific (SP), southeastern Pacific (SEPAC), and South Atlantic (SATL). The longitude boundaries of the Northern Hemisphere basins are as defined for modern-day WMO Regional Specialized Meteorological Centers. Longitude bounds for the Southern Hemisphere are defined from the coast of Africa through 130°E for SI, from 130°E through 120°W for SP, from 120°W to the South American coastline for SEPAC, and including the entire basin for SATL. Latitude bounds extend from the equator to the poles.

c. *Seasonal cycle and season length*

The annual cycle of storm genesis for each model is shown in Fig. 6. In both climates and in all three models, July–October (JASO) is the most active period in the Northern Hemisphere, and January–April the most active in the Southern Hemisphere, and for this reason we have used these months to define the ''storm seasons'' for each hemisphere throughout the paper. On closer inspection, there are some subtle differences in the timing of genesis between C20 and LGM: in all three models and in both hemispheres, the median day of genesis occurs about one week earlier in LGM than in C20 (Table 2).[5] In CCSM and MPI, Northern Hemisphere activity declines in all months at LGM, but the decrease at the end of the season (November) is steeper than in the rest of the season. Activity during the early months of the season (May and June) decreases by a smaller percentage. Similarly, CCSM and MPI show robust early season Southern Hemisphere activity in the LGM in December, whereas April and May show steep declines, particularly in CCSM. MRI, which has an overall increase in LGM storm frequency, also has a shift in the median genesis day to earlier in the season. LGM activity in MRI is elevated from June through September relative to C20 and shows small declines in October and November. The Southern Hemisphere season in MRI also shows increased LGM activity during November and December with a small decline in April. Using the same TC downscaling methodology employed here, Dwyer et al. (2015) reported a phase shift of the TC climatology toward later in the year for warmer Coupled Model Intercomparison Project phase 3 (CMIP3) and phase 5 (CMIP5) projections; this is consistent with the earlier shift of the date of median activity seen in these colder LGM simulations. Earlier autumnal terminations for TC activity appear to be associated with high wind shear and the equatorward retreat of high potential intensity during the autumn months (not shown). The areal extent of favorable potential intensity is smaller in the LGM than in the C20 simulations, and this area contracts earlier in the autumn season in the LGM (Fig. 1d).

4. Environmental conditions in twentieth-century simulations

In the last section, we showed that the fraction of TCs that reach H4 or higher intensity is smaller in LGM than 20C in all models, and that the median day of the season is earlier by an average of a week in all models and in both hemispheres. However, there were also obvious intermodel differences that impact the total storm count and, as we detail in the next section, distributions by basin. In this section we pause to compare the C20 simulations of each model to reanalysis data, as this provides an important context to interpreting the individual model responses at LGM.

The left panels of Figs. 7a–d compare SST from the Extended Reconstructed Sea Surface Temperature version 5 (ERSST) averaged over July to October for the period 1980–2005 (the same period analyzed for C20 experiments) and departures from it for each of the three C20 models. CCSM has lower JASO SSTs than climatology across the tropical North Atlantic (east of the Caribbean Sea to the coast of Africa), SSTs warmer than climatology in the eastern tropical North Pacific, and temperatures near climatology in the tropical western North Pacific. MPI anomalies are lower than CCSM in the Pacific but have a similar pattern. MRI has larger cold anomalies in both the western North Pacific and in the North Atlantic basin.

One way to gauge how differences in SST between C20 simulations and the observed climatology could affect TCs is to calculate the relative SST (RSST), which is the deviation of

[5] Here we have not calendar-adjusted the output but note that the impact of changes in Earth's orbital characteristics only result in errors of about a day at the LGM (Bartlein and Shafer 2019). Conclusions based on changes on the order of a week, as shown here, should still hold.

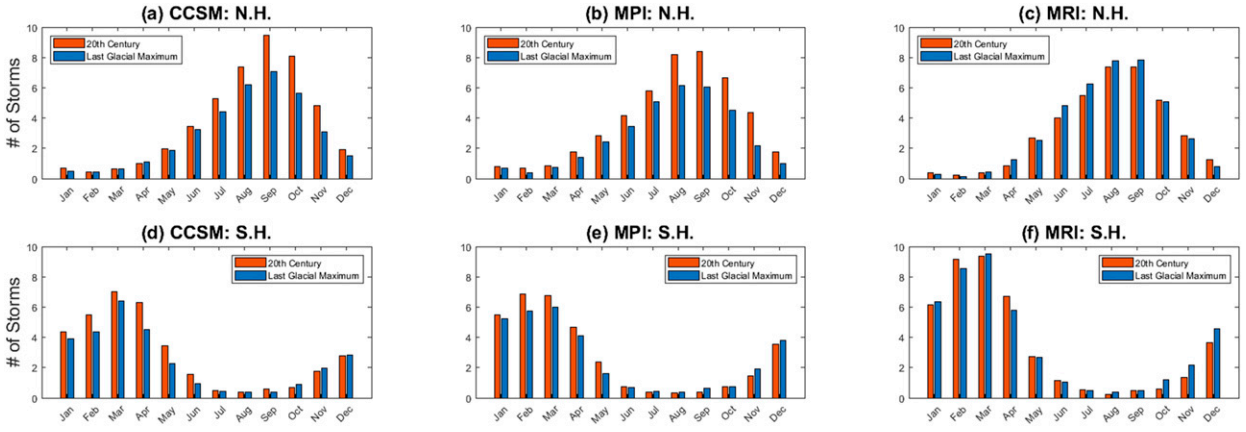

FIG. 6. Annual cycle of TC frequency. (a) Northern Hemisphere of CCSM; (b) Northern Hemisphere of MPI; (c) Northern Hemisphere of MRI. (d)–(f) As in (a)–(c), but for the Southern Hemisphere.

local SST from the tropical mean; it is highly correlated with potential intensity (Vecchi and Soden 2007). In the ERSST climatology, the highest RSST is found in the western North Pacific, where SST is more than 2°C warmer in the JASO mean than the average of the Northern Hemisphere tropics in JASO (Fig. 7e).[6] The western part of the Atlantic basin is also more than 1°C warmer during JASO than the average between the equator and 30°N during the same months. Deviations in a model's C20 RSST field from the RSST of the ERSST climatology (Figs. 7f–h) are qualitatively similar to the deviations of each model's SST field from the observational climatology (Figs. 7b–d). Across much of the tropical North Pacific, CCSM and MPI show similar anomalies, but the there is significant cool bias in the Atlantic in CCSM. The western North Pacific and Atlantic are anomalously cool in the C20 of MRI, while the eastern and central Pacific are relatively too warm. As shown later, this different RSST pattern affects the distribution of TCs generated in MRI C20 compared to actual genesis regions in observations.

Figure 8 shows PI changes at LGM at each ocean grid point as a function of changes in RSST (including points between the equator and 30°N during JASO) from C20 to LGM. Here we have filtered points so that only those whose JASO seasonal PI averages exceed 55 m s^{-1} in either C20 or LGM are shown. Korty et al. (2012a,b) showed that this threshold in PI approximately separates points where deep convection is possible from those where vertical soundings cap convection in the lower troposphere. Points to the right of the vertical line have a warmer RSST in LGM than in C20, and generally have larger PI at LGM; those to the left of the line have colder RSST at LGM (all points have colder absolute SST) with generally lower PI at LGM. There are some exceptions to this relationship, particularly when the magnitude of RSST or PI changes are small and in CCSM. Nevertheless, it demonstrates the close relationship between PI and RSST changes in these model simulations.

High vertical wind shear is another significant obstacle to TC genesis, and the magnitude of the deep layer shear vector (850–250 hPa) is an important parameter in many TC genesis indices. The vector difference averaged over JASO is dominated by variability in the magnitude of the larger 250-hPa wind speed, and its 1980–2005 average in the National Centers for Environmental Prediction (NCEP)–National Center for Atmospheric Research (NCAR) reanalysis is shown in Fig. 9a. The genesis regions for most Atlantic and Pacific TCs feature climatologically low wind speeds aloft, while regions with stronger upper-level wind speeds (e.g., near and northeast of Hawaii) generate few TCs. Differences in 250-hPa JASO wind speed magnitude in each model's C20 simulation are shown in Figs. 9b–d. Departures from climatology are qualitatively similar in the tropics of all models: generally weaker wind speeds west of the Philippines, near Hawaii, and in parts of the low-latitude eastern North Pacific, while wind speeds are higher in each of the three models across the tropical North Atlantic and Gulf of Mexico. Yet the magnitudes are significantly higher in MRI than in other models, and coupled with SST (and RSST) values that are too low in the tropical North Atlantic, C20 conditions are far less favorable in the Atlantic of this model than they are in observations. Reanalysis of September data shows a westerly jet at 250 hPa along the coast of West Africa near 30°–35°N, but this maximum is stronger and located 10° latitude to the south in MRI's C20. This shift in position and intensity is concurrent with an anomalously strong horizontal temperature gradient over North Africa in MRI (not shown), which is at least in part related to the reduction in basin wide SSTs. These departures from

[6] Here we use the mean SST between the equator and 30°N to define the "Northern Hemisphere tropical mean" temperature. Other studies have used a wider tropical mean between 30°S and 30°N from which to calculate RSST anomalies; making that choice here would alter only the magnitude of the RSST, not its spatial pattern.

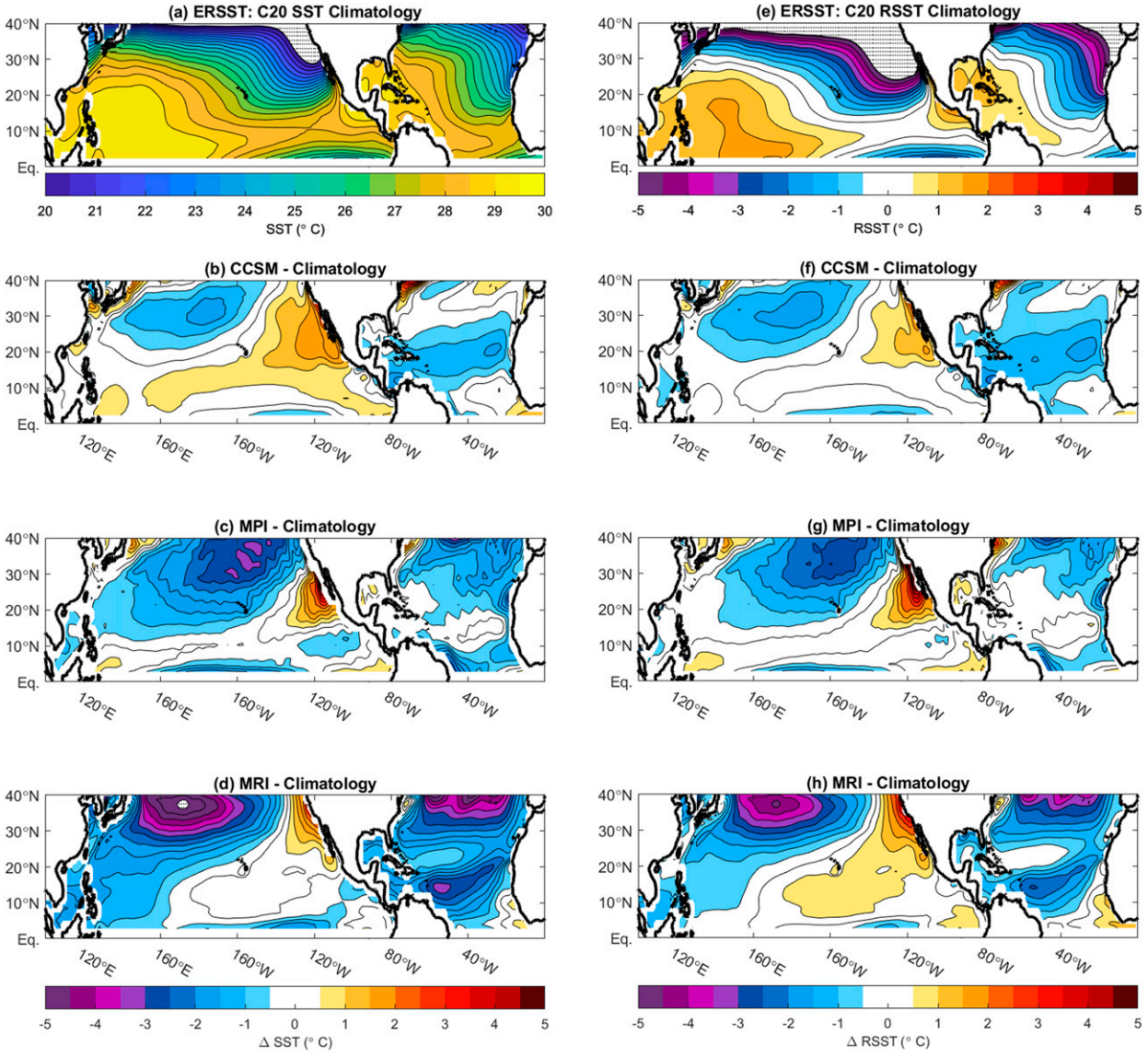

FIG. 7. Comparison of ERSST reanalysis and each C20 simulation. (a) Average SST for Northern Hemisphere storm season (July–October) from 1980 to 2005. (b) Deviation of CCSM's C20 SST field from ERSST climatology shown in (a). (c), (d) As in (b), but for MPI and MRI, respectively. (e) Average RSST (computed by subtracting 0°–30°N storm season SST mean) in ERSST climatology from 1980 to 2005. (f)–(h) As in (b)–(d), but showing deviations of each model's C20 RSST field from the ERSST climatology shown in (e). Dotted white regions indicate areas where values were colder than the plotted contours.

climatology are instructive in understanding some of the regional variations of the responses, which we consider in the next section.

5. Intermodel variability

We compare the LGM responses of downscaled TCs between the three models and focus on regional differences in several basins, illustrating that intermodel variability can result in very different TC responses even when the global forcing driving the model is identical.

a. North Atlantic

Figure 10 shows the difference in PDI in the North Atlantic (integrated over the entire year, but dominated by activity during JASO), along with changes in JASO CGI, PI, and vertical wind shear. There is a strong correspondence between each model's LGM response and the changes in environmental conditions. Both CCSM and MPI have lower Atlantic activity at LGM, and both have lower PI, higher shear, and a less favorable CGI across much of the basin. By contrast, MRI has higher Atlantic activity at LGM, driven by higher PI, lower shear, and larger CGI across the tropical latitudes of the basin.

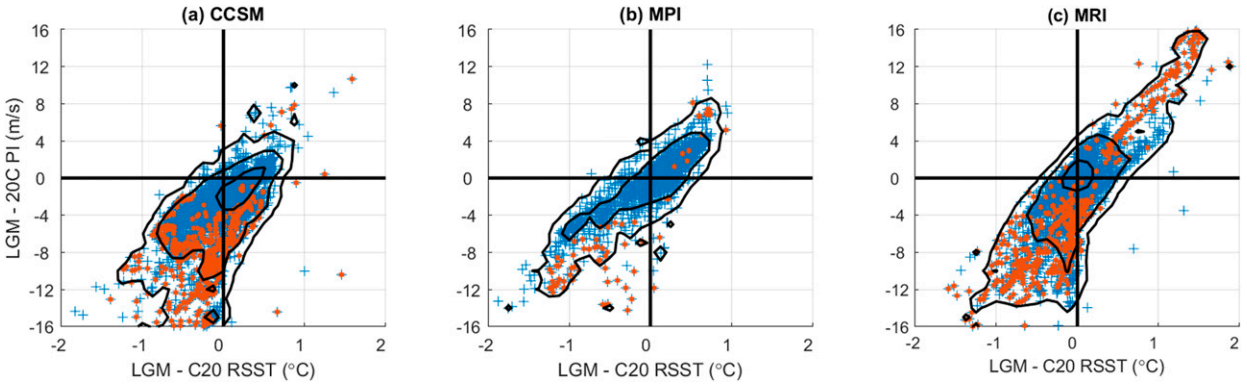

FIG. 8. Scatterplot of JASO LGM − C20 RSST vs LGM − C20 potential intensity (PI) at each grid point in the Northern Hemisphere for (a) CCSM, (b) MPI, and (c) MRI. Only points where potential intensity exceeds 55 m s^{-1} in either climate are shown; hexagonal orange markers indicate points where potential intensity was greater than 55 m s^{-1} in one climate but not the other, while blue pluses indicate it was greater than 55 m s^{-1} in both climates. Overlain contours are of the scatter point density—using 32^2 equally spaced bins and passed through a Gaussian filter (sigma = 0.5)—at increasing intervals of 1, 10, and 100.

We showed that MRI simulates colder SST in the Atlantic in its C20 simulation than is observed in nature (cf. Fig. 7d). Zhang and Wang (2013) diagnosed the strength of the Atlantic meridional overturning circulation (AMOC) in the historical run of each model's C20 simulation, and tied changes in its intensity to Atlantic meridional variability (AMV) and simulated SSTs. MRI simulates a weaker AMOC in C20 than does CCSM or MPI (cf. their Fig. 6) and simulated SSTs deviate from observations most strongly in middle and high latitudes of the North Atlantic (see Fig. 7d). Muglia and Schmittner (2015) compare the changes in simulated AMOC strength between preindustrial era control runs and LGM simulations, and report that MRI had a larger increase in AMOC intensity from its preindustrial era run than did either CCSM or MPI. All three models simulate strong AMOC (~21–22 Sv; 1 Sv ≡ 10^6 m^3 s^{-1}) in their LGM simulations, while there is significant variability in the intensity of their preindustrial era strengths (20 Sv in CCSM, 18 Sv in MPI, and only 15 Sv in MRI). Thus, the large increase in AMOC strength in the LGM simulation of MRI is principally because its contemporary simulation has a much weaker circulation than other models do. Weaker AMOC circulations have been tied to cooler Atlantic SSTs throughout the Northern Hemisphere (Muir and Fedorov 2015), which is consistent with the C20 pattern seen in MRI. We note, however, that other decades of MRI's LGM simulation had weaker AMOC than in the 30 years available for downscaling (i.e., those with daily wind data saved). Those years have lower RSST in much of the Atlantic basin, particularly in the subtropics and western Atlantic (not shown), and this natural variability likely would have altered the TC climatology.

b. Western North Pacific

Downscaled TCs display less intermodel variability in the western North Pacific than in the North Atlantic, but because it is the most active basin and the largest contributor to the global total, we examine some details of each model's responses and differences here. Figure 11 shows the changes in PDI, CGI, PI, and shear at LGM for each of the three models in our ensemble. The composite genesis, track, and PDI density changes (shown in Figs. 3 and 4) indicate a decrease in activity in the westernmost part of the basin near the Asian continent, with small or slightly positive differences at LGM farther east in the basin. The top row of Fig. 11 shows that each of the three models show decreases in PDI near the continent, with some variability in the response farther east. In the western North Pacific, changes in CGI do not capture this variability in PDI as well as other basins due to additional intermodel variability in midlevel moisture. For example, in the region from 160°E–180°, MPI had drier midlevel relative humidity at LGM despite higher CGI, and near the Asian coastline increased relative humidity at LGM in CCSM and MRI may have offset less favorable PI and shear (not shown).

Potential intensity is little changed across wide swaths of the west Pacific warm pool in each of the LGM simulations and is higher in the central Pacific in MPI. Wind shear, however, is larger in all three models near the coastline of Asia. Elevated shear results from increases in upper-level winds (e.g., 250 hPa) near the coastline, and appears to be a consequence of stronger land–sea temperature gradients in thermal wind balance with higher shears during the summer months of each LGM simulation; vegetation cover on the exposed Sunda and Sahul Shelves can also affect the Walker circulation and shear (DiNezio et al. 2011, 2018; DiNezio and Tierney 2013). Extensive ice coverage at high latitudes resulted in lower global sea levels, exposing a larger land area of the Maritime Continent during the LGM (Braconnot et al. 2012). During the late summer months, a larger horizontal temperature gradient develops between the Maritime Continent and the adjacent Pacific Ocean waters in each LGM simulation, driving larger vertical

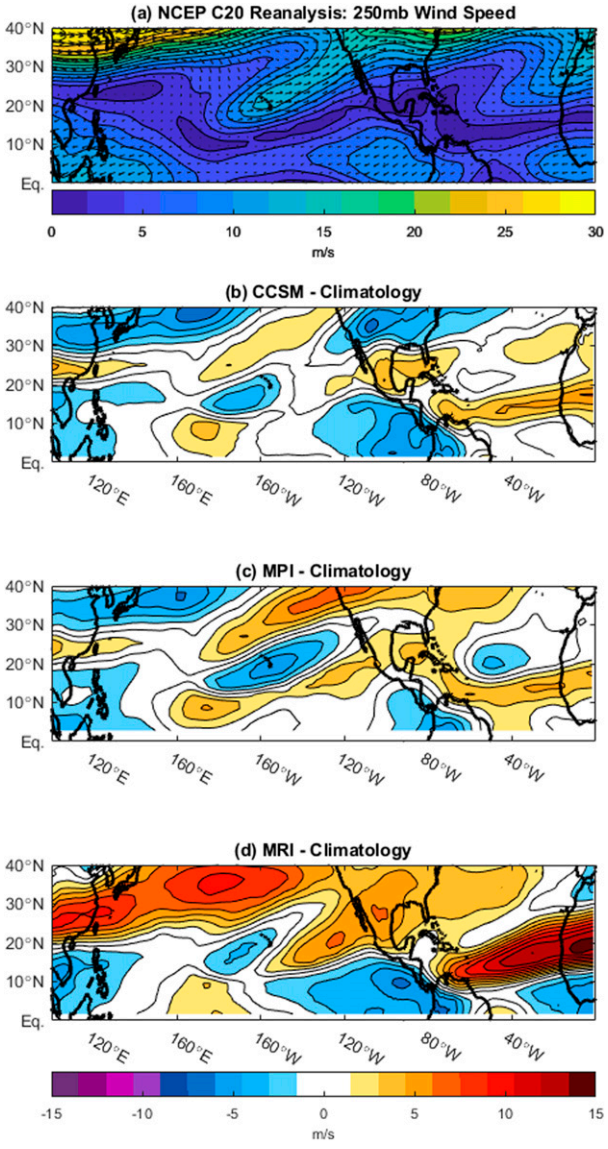

FIG. 9. (a) NCEP–NCAR reanalysis 250-hPa wind vectors and speed (contours) averaged over July–October from 1980 to 2005. (b) Deviation of CCSM's C20 storm season wind speed at 250 hPa from climatology shown in (a). (c),(d) As in (b), but for MPI and MRI, respectively.

shears than in the C20 simulations. PDI is lower in all three models' LGM simulations near the Asian coastline, but storm track density and PDI (cf. Figs. 4b,d) increase farther offshore as storms are steered poleward earlier in their tracks.

c. *Other ocean basins*

Briefly, we present some details from other regions of the world. In the northern Indian Ocean, PDI density was reduced at LGM (cf. Fig. 3) in the three-model composite. PI was generally lower while shear was higher in each LGM simulation. In the Bay of Bengal, the PDI at LGM showed no significant change in MPI but decreased from C20 in the other two models. Variability in this basin had little effect on global TC count (Fig. 5). At LGM, all three models showed in the eastern North Pacific a poleward expansion of the region with high PI (cf. composite shown in Fig. 1d), but this was also accompanied by an increase in mean wind shear (not shown). Changes in PDI were mixed between the models, with MPI producing an increase at LGM and the others showing slight differences. Variability in these basins was not large enough to significantly alter global TC counts (Fig. 5).

There is also noteworthy variability in the Southern Hemisphere, particularly in the Indian and South Pacific basins. TCs downscaled from CCSM displayed the greatest reduction in PDI at LGM, and the number of TCs was also significantly lower in this hemisphere (Fig. 5). CCSM's LGM simulation featured a larger increase in wind shear off of the west coast of Australia than did the other two models (which instead depicted a decrease in wind shear) and also had the greatest reduction in PI in the southern Pacific (not shown). Rojas (2013) noted that CCSM and MRI were the only two of eight models they examined whose LGM simulations showed poleward shifts and increases in intensity of the Southern Hemisphere jet. The differences in shear associated with the position of the jets can affect the conduciveness for TCs on the subtropical margin of TC formation regions.

6. Conclusions

Tropical cyclones downscaled from simulations of the LGM show that despite significantly colder conditions, glacial climates can support and sustain a climatology of tropical storms in many of the same regions in which they are found in modern times. Yet there are also substantial changes in the frequency, intensity distribution, and seasonal cycle of TCs that are broadly consistent with changes seen in warmer projections of the late twenty-first century. Storms at LGM were less frequent and less intense in two of the three models we examined, and all three models showed a decline in the fraction of total storms that reach the highest categories of intensity. The median day for storm genesis shifted by an average of one week earlier in both the Northern and Southern Hemispheres of all three models.

Our LGM results show consistency with several responses seen in simulations of many warmer climates, both projections of future warming (Emanuel 2013) as well as very hot climates (Korty et al. 2017). These include an increase in the fraction and frequency of the strongest storms with warming, a shift in the median day of activity to later in the storm season with warming (e.g., Dwyer et al. 2015), and a general trend toward more total storms with warming. There is a consistent shift in late season Northern Hemisphere activity: here we find a decrease in October and November storm frequency in colder climates, and Korty et al. (2017) found increases during these months in simulations of very hot climates. The total count is more complicated: in these cold climates, we find a ~12%

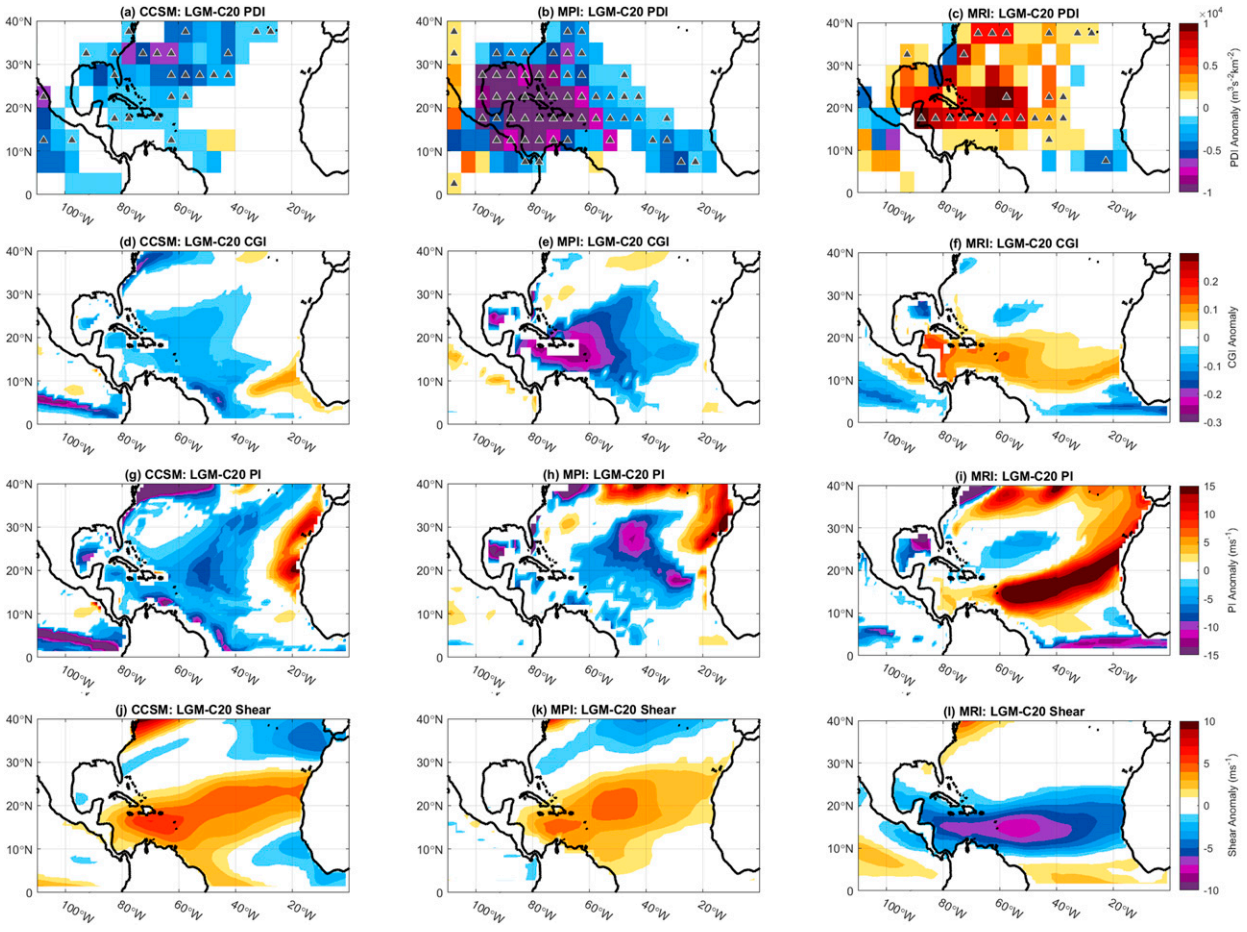

FIG. 10. Differences between LGM and C20 North Atlantic TC power dissipation and environmental conditions. (a) Difference in PDI ($m^3 s^{-2} km^{-2}$) between LGM and C20 in CCSM. Grid boxes with statistically significant differences (at 95% confidence threshold) are shown with a black triangle. (b),(c) As in (a), but for MPI and MRI, respectively. (d) Differences in CGI between LGM and C20 for CCSM averaged over the storm-season (JASO). Only changes that are statistically significant are contoured. (e),(f) As in (d), but for MPI and MRI, respectively. (g)–(i) As in (d)–(f), but for potential intensity. (j)–(l) As in (d)–(f), but for 850–250-hPa shear.

decline in count averaged over this ensemble (but one model had no significant change). Emanuel (2013) reported increases of ~25% averaged over an ensemble of transient CMIP5 model projections by the end of the twenty-first century, although in equilibrium simulations Korty et al. (2017) showed smaller increases in much hotter cases with 8 and 32 times preindustrial era levels of carbon dioxide (+16% and +20%, respectively). Note, however, that the storm count using this downscaling method behaves differently from count changes of directly simulated storms: their count most often declines with warming (Sobel et al. 2016; Walsh et al. 2016), although some simulations do not (Vecchi et al. 2019).

It is also clear that regional variability, particularly in the North Atlantic, can alter any one model's global response substantially, and that large intermodel variability can exist within any ensemble of a particular climate scenario. While two of the three models showed declines in global PDI at LGM, a third showed no significant change. Its North Atlantic conditions are far less conducive for storm formation in its C20 simulation than are actual contemporary environmental conditions in this basin, and the number of seed vortices required to generate a modern climatology for this model was larger. Subtle differences in the relative magnitude of SST can impart a large effect on the TC climatology, and careful study of biases in control climate simulations should be examined to aid understanding of changes seen in future or past climate change scenarios.

We caution against interpolating these results to other cool periods, such as the Little Ice Age (LIA) that occurred during the middle of the last millennium. Although there are a growing number of proxy storm records from LIA, these records cannot be compared directly with our work on the LGM, as the reasons why the LIA was colder differ from the LGM. TCs respond to volcanism or to changes in the solar constant very differently than they do to changes in carbon dioxide or to the large-scale circulation changes that result from large continental ice sheets (e.g., Korty et al. 2012b; Emanuel and Sobel 2013). The response of TCs during colder intervals of the last millennium will be driven by different external forces than

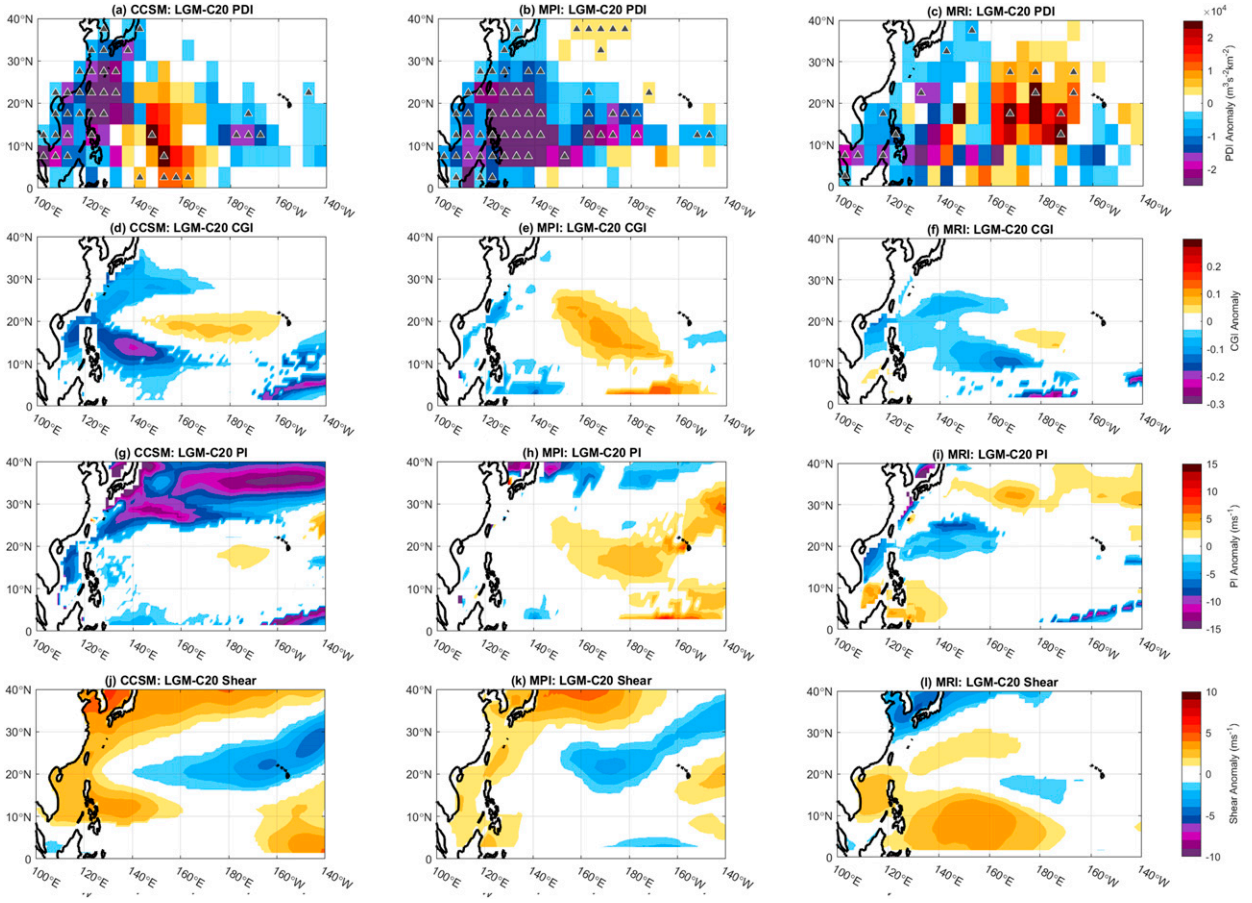

FIG. 11. As in Fig. 10, but for the western North Pacific.

were these simulations of the LGM, and they are worthy of investigation in their own right.

Acknowledgments. We thank Kerry Emanuel for generating the event sets for these simulations, and we thank the climate modeling groups for producing and sharing output from their simulations through the Paleoclimate and Coupled Model Intercomparison Project. We appreciate the helpful comments from Chris Brierley and two anonymous reviewers, which substantially improved the paper. Support was provided by National Science Foundation Grants AGS-1064013 and ICER-1854917.

Data availability statement. Data necessary to reconstruct figures for downscaled TCs and those of derived (PI, CGI, shear) environmental fields are available at https://doi.org/10.17605/OSF.IO/5DJF9. The full set of downscaled tropical cyclone tracks used in this study are freely available for research purposes only by contacting Kerry Emanuel (emanuel@mit.edu). PMIP3 climate data are available at https://esgf.llnl.gov/index.html (see Braconnot et al. 2012). Climatological sea surface temperature data used in this study are from the ERSST dataset and available at https://doi.org/10.7289/V5T72FNM (see Huang et al. 2017). NCEP–NCAR reanalysis products (Kalnay et al. 1996) are available at https://psl.noaa.gov/.

REFERENCES

Abe-Ouchi, A., and Coauthors, 2015: Ice-sheet configuration in the CMIP5/PMIP3 Last Glacial Maximum experiments. *Geosci. Model Dev.*, **8**, 3621–3637, https://doi.org/10.5194/gmd-8-3621-2015.

Annan, J. D., and J. C. Hargreaves, 2013: A new global reconstruction of temperature changes at the Last Glacial Maximum. *Climate Past*, **9**, 367–376, https://doi.org/10.5194/cp-9-367-2013.

Anthes, R. A., 1982: *Tropical Cyclones, Their Evolution, Structure and Effects*. American Meteorological Society, 208 pp.

Bartlein, P. J., and S. L. Shafer, 2019: Paleo calendar-effect adjustments in time-slice and transient climate-model simulations (PaleoCalAdjust v1.0): Impact and strategies for data analysis. *Geosci. Model Dev.*, **12**, 3889–3913, https://doi.org/10.5194/gmd-12-3889-2019.

Bister, M., and K. A. Emanuel, 2002: Low frequency variability of tropical cyclone potential intensity: 1. Interannual to interdecadal variability. *J. Geophys. Res.*, **107**, 4801, https://doi.org/10.1029/2001JD000776.

Braconnot, P., S. P. Harrison, M. Kageyama, P. J. Bartlein, V. Masson-Delmotte, A. Abe-Ouchi, B. Otto-Bliesner, and Y. Zhao, 2012: Evaluation of climate models using palaeoclimatic data. *Nat. Climate Change*, **2**, 417–424, https://doi.org/10.1038/nclimate1456.

Brady, E. C., B. L. Otto-Bliesner, J. E. Kay, and N. Rosenbloom, 2013: Sensitivity to glacial forcing in the CCSM4. *J. Climate*, **26**, 1901–1925, https://doi.org/10.1175/JCLI-D-11-00416.1.

Bruyère, C. L., G. J. Holland, and E. Trowler, 2012: Investigating the use of a genesis potential index for tropical cyclones in the North Atlantic basin. *J. Climate*, **25**, 8611–8626, https://doi.org/10.1175/JCLI-D-11-00619.1.

Camargo, S. J., 2013: Global and regional aspects of tropical cyclone activity in the CMIP5 models. *J. Climate*, **26**, 9880–9902, https://doi.org/10.1175/JCLI-D-12-00549.1.

——, and A. A. Wing, 2016: Tropical cyclones in climate models. *Wiley Interdiscip. Rev. Climate Change*, **7**, 211–237, https://doi.org/10.1002/wcc.373.

——, A. H. Sobel, A. G. Barnston, and K. A. Emanuel, 2007: Tropical cyclone genesis potential index in climate models. *Tellus*, **59A**, 428–443, https://doi.org/10.1111/j.1600-0870.2007.00238.x.

DeMaria, M., 1996: The effect of vertical shear on tropical cyclone intensity change. *J. Atmos. Sci.*, **53**, 2076–2088, https://doi.org/10.1175/1520-0469(1996)053<2076:TEOVSO>2.0.CO;2.

DiNezio, P. N., and J. Tierney, 2013: The effect of sea level on glacial Indo-Pacific climate. *Nat. Geosci.*, **6**, 485–491, https://doi.org/10.1038/ngeo1823.

——, A. C. Clement, G. A. Vecchi, B. J. Soden, A. J. Broccoli, B. L. Otto-Bliesner, and P. Braconnot, 2011: The response of the Walker circulation to Last Glacial Maximum forcing: Implications for detection in proxies. *Paleoceanography*, **26**, PA3217, https://doi.org/10.1029/2010PA002083.

——, J. E. Tierney, B. L. Otto-Bliesner, A. Timmermann, T. Bhattacharya, N. Rosenbloom, and E. Brady, 2018: Glacial changes in tropical climate amplified by the Indian Ocean. *Sci. Adv.*, **4**, eaat9658, https://doi.org/10.1126/sciadv.aat9658.

Dwyer, J. G., S. J. Camargo, A. H. Sobel, M. Biasutti, K. A. Emanuel, G. A. Vecchi, M. Zhao, and M. K. Tippett, 2015: Projected twenty-first-century changes in the length of the tropical cyclone season. *J. Climate*, **28**, 6181–6192, https://doi.org/10.1175/JCLI-D-14-00686.1.

Emanuel, K. A., 1987: The dependence of hurricane intensity on climate. *Nature*, **326**, 483–485, https://doi.org/10.1038/326483a0.

——, 1995: The behavior of a simple hurricane model using a convective scheme based on subcloud-layer entropy equilibrium. *J. Atmos. Sci.*, **52**, 3960–3968, https://doi.org/10.1175/1520-0469(1995)052<3960:TBOASH>2.0.CO;2.

——, 2005: Increasing destructiveness of tropical cyclones over the past 30 years. *Nature*, **436**, 686–688, https://doi.org/10.1038/nature03906.

——, 2006: Climate and tropical cyclone activity: A new model downscaling approach. *J. Climate*, **19**, 4797–4802, https://doi.org/10.1175/JCLI3908.1.

——, 2013: Downscaling CMIP5 climate models shows increased tropical cyclone activity over the 21st century. *Proc. Natl. Acad. Sci. USA*, **110**, 12 219–12 224, https://doi.org/10.1073/pnas.1301293110.

——, and D. S. Nolan, 2004: Tropical cyclone activity and global climate. Preprints, *26th Conf. on Hurricanes and Tropical Meteorology*, Miami, FL, Amer. Meteor. Soc., 240–241.

——, and A. Sobel, 2013: Response of tropical sea surface temperature, precipitation, and tropical cyclone-related variables to changes in global and local forcing. *J. Adv. Model. Earth Syst.*, **5**, 447–458, https://doi.org/10.1002/jame.20032.

——, C. DesAutels, C. Holloway, and R. Korty, 2004: Environmental control of tropical cyclone intensity. *J. Atmos. Sci.*, **61**, 843–858, https://doi.org/10.1175/1520-0469(2004)061<0843:ECOTCI>2.0.CO;2.

——, R. Sundararajan, and J. Williams, 2008: Hurricanes and global warming: Results from downscaling IPCC AR4 simulations. *Bull. Amer. Meteor. Soc.*, **89**, 347–368, https://doi.org/10.1175/BAMS-89-3-347.

Fedorov, A. V., C. M. Brierley, and K. Emanuel, 2010: Tropical cyclones and permanent El Niño in the early Pliocene epoch. *Nature*, **463**, 1066–1070, https://doi.org/10.1038/nature08831.

Frank, W. M., and G. S. Young, 2007: The interannual variability of tropical cyclones. *Mon. Wea. Rev.*, **135**, 3587–3598, https://doi.org/10.1175/MWR3435.1.

Gray, W. M., 1968: Global view of the origin of tropical disturbances and storms. *Mon. Wea. Rev.*, **96**, 669–700, https://doi.org/10.1175/1520-0493(1968)096<0669:GVOTOO>2.0.CO;2.

Harrison, S. P., and Coauthors, 2014: Climate model benchmarking with glacial and mid-Holocene climates. *Climate Dyn.*, **43**, 671–688, https://doi.org/10.1007/s00382-013-1922-6.

——, P. J. Bartlein, K. Izumi, G. Li, J. Annan, J. Hargreaves, P. Braconnot, and M. Kageyama, 2015: Evaluation of CMIP5 palaeo-simulations to improve climate projections. *Nat. Climate Change*, **5**, 735–743, https://doi.org/10.1038/nclimate2649.

Hobgood, J. S., and R. S. Cerveny, 1988: Ice-age hurricanes and tropical storms. *Nature*, **333**, 243–245, https://doi.org/10.1038/333243a0.

Huang, B., and Coauthors, 2017: NOAA Extended Reconstructed Sea Surface Temperature (ERSST), version 5. NOAA National Centers for Environmental Information, accessed 21 March 2019, https://doi.org/10.7289/V5T72FNM.

Kalnay, E., and Coauthors, 1996: The NCEP/NCAR 40-Year Reanalysis Project. *Bull. Amer. Meteor. Soc.*, **77**, 437–471, https://doi.org/10.1175/1520-0477(1996)077<0437:TNYRP>2.0.CO;2.

Knutson, T., and Coauthors, 2019: Tropical cyclones and climate change assessment: Part I: Detection and attribution. *Bull. Amer. Meteor. Soc.*, **100**, 1987–2007, https://doi.org/10.1175/BAMS-D-18-0189.1.

——, and Coauthors, 2020: Tropical cyclones and climate change assessment: Part II: Projected response to anthropogenic warming. *Bull. Amer. Meteor. Soc.*, **101**, E303–E322, https://doi.org/10.1175/BAMS-D-18-0194.1.

Koh, J. H., and C. M. Brierley, 2015: Tropical cyclone genesis potential across palaeoclimates. *Climate Past*, **11**, 1433–1451, https://doi.org/10.5194/cp-11-1433-2015.

Korty, R. L., and K. A. Emanuel, 2007: The dynamic response of the winter stratosphere to an equable climate surface temperature gradient. *J. Climate*, **20**, 5213–5228, https://doi.org/10.1175/2007JCLI1556.1.

——, ——, and J. R. Scott, 2008: Climatology of the tropospheric thermal stratification using saturation potential vorticity. *J. Climate*, **20**, 5977–5991, https://doi.org/10.1175/2007JCLI1788.1.

——, S. J. Camargo, and J. Galewsky, 2012a: Tropical cyclone genesis factors in simulations of the Last Glacial Maximum. *J. Climate*, **25**, 4348–4365, https://doi.org/10.1175/JCLI-D-11-00517.1.

——, ——, and ——, 2012b: Variations in tropical cyclone genesis factors in simulations of the Holocene epoch. *J. Climate*, **25**, 8196–8211, https://doi.org/10.1175/JCLI-D-12-00033.1.

——, K. A. Emanuel, M. Huber, and R. Zamora, 2017: Tropical cyclones downscaled from simulations with very high carbon dioxide levels. *J. Climate*, **30**, 649–667, https://doi.org/10.1175/JCLI-D-16-0256.1.

Kossin, J. P., 2018: A global slowdown of tropical-cyclone translation speed. *Nature*, **558**, 104–107, https://doi.org/10.1038/s41586-018-0158-3.

——, K. A. Emanuel, and G. A. Vecchi, 2014: The poleward migration of the location of tropical cyclone maximum intensity. *Nature*, **509**, 349–352, https://doi.org/10.1038/nature13278.

Lee, C.-Y., S. J. Camargo, A. H. Sobel, and M. K. Tippett, 2020: Statistical-dynamical downscaling projections of tropical cyclone activity in a warming climate: Two diverging genesis scenarios. *J. Climate*, **33**, 4815–4834, https://doi.org/10.1175/JCLI-D-19-0452.1.

Muglia, J., and A. Schmittner, 2015: Glacial Atlantic overturning increased by wind stress in climate models. *Geophys. Res. Lett.*, **42**, 9862–9869, https://doi.org/10.1002/2015GL064583.

Muir, L. C., and A. V. Fedorov, 2015: How the AMOC affects ocean temperatures on decadal to centennial timescales: the North Atlantic versus an interhemispheric seesaw. *Climate Dyn.*, **45**, 151–160, https://doi.org/10.1007/s00382-014-2443-7.

Nolan, D., 2011: Evaluating environmental favorableness for tropical cyclone development with the method of point-downscaling. *J. Adv. Model. Earth Syst.*, **3**, M08001, https://doi.org/10.1029/2011MS000063.

Palmen, E., 1948: On the formation and structure of tropical cyclones. *Geophysica*, **3**, 26–38.

Pausata, F. S. R., K. A. Emanuel, M. Chiacchio, G. T. Diro, Q. Zhang, L. Sushama, J. C. Stager, and J. P. Donnelly, 2017: Tropical cyclone activity enhanced by Sahara greening and reduced dust emissions during the African Humid Period. *Proc. Natl. Acad. Sci. USA*, **114**, 6221–6226, https://doi.org/10.1073/pnas.1619111114.

Rojas, M., 2013: Sensitivity of Southern Hemisphere circulation to LGM and 4xCO2 climates. *Geophys. Res. Lett.*, **40**, 965–970, https://doi.org/10.1002/grl.50195.

Royer, J.-F., F. Chauvin, B. Timbal, P. Araspin, and D. Grimal, 1998: A GCM study of the impact of greenhouse gas increase on the frequency of occurrence of tropical cyclones. *Climatic Change*, **38**, 307–343, https://doi.org/10.1023/A:1005386312622.

Sobel, A. H., S. J. Camargo, T. M. Hall, C.-Y. Lee, M. K. Tippett, and A. A. Wing, 2016: Human influence on tropical cyclone intensity. *Science*, **353**, 242–246, https://doi.org/10.1126/science.aaf6574.

Tang, B., and K. Emanuel, 2010: Midlevel ventilation's constraint on tropical cyclone intensity. *J. Atmos. Sci.*, **67**, 1817–1830, https://doi.org/10.1175/2010JAS3318.1.

——, and ——, 2012: A ventilation index for tropical cyclones. *Bull. Amer. Meteor. Soc.*, **93**, 1901–1912, https://doi.org/10.1175/BAMS-D-11-00165.1.

Tippett, M. K., S. J. Camargo, and A. H. Sobel, 2011: A Poisson regression index for tropical cyclone genesis and the role of large-scale vorticity in genesis. *J. Climate*, **24**, 2335–2357, https://doi.org/10.1175/2010JCLI3811.1.

Toomey, M. R., W. B. Curry, J. P. Donnelly, and P. J. van Hengstum, 2013: Reconstructing 7000 years of North Atlantic hurricane variability using deep-sea sediment cores from the western Great Bahama Bank. *Paleoceanography*, **28**, 31–41, https://doi.org/10.1002/palo.20012.

——, R. L. Korty, J. P. Donnelly, P. J. van Hengstum, and W. B. Curry, 2017: Increased hurricane frequency near Florida during Younger Dryas Atlantic meridional overturning circulation slowdown. *Geology*, **45**, 1047–1050, https://doi.org/10.1130/G39270.1.

van Hengstum, P. J., T. S. Winkler, A. E. Tamalavage, R. M. Sullivan, S. N. Little, D. MacDonald, J. P. Donnelly, and N. A. Albury, 2020: Holocene sedimentation in a blue hole surrounded by carbonate tidal flats in the Bahamas: Autogenic versus allogenic processes. *Mar. Geol.*, **419**, 106051, https://doi.org/10.1016/j.margeo.2019.106051.

Vecchi, G. A., and B. J. Soden, 2007: Effect of remote sea surface temperature change on tropical cyclone potential intensity. *Nature*, **450**, 1066–1070, https://doi.org/10.1038/nature06423.

——, and Coauthors, 2019: Tropical cyclone sensitivities to CO_2 doubling: Roles of atmospheric resolution, synoptic variability and background climate changes. *Climate Dyn.*, **53**, 5999–6033, https://doi.org/10.1007/s00382-019-04913-y.

Walsh, K. J. E., and Coauthors, 2016: Tropical cyclones and climate change. *Wiley Interdiscip. Rev. Climate Change*, **7**, 65–89, https://doi.org/10.1002/wcc.371.

Webster, P. J., G. J. Holland, J. A. Curry, and H.-R. Chang, 2005: Changes in tropical cyclone number, duration, and intensity in a warming environment. *Science*, **309**, 1844–1846, https://doi.org/10.1126/science.1116448.

Xu, K.-M., and K. A. Emanuel, 1989: Is the tropical atmosphere conditionally unstable? *Mon. Wea. Rev.*, **117**, 1471–1479, https://doi.org/10.1175/1520-0493(1989)117<1471:ITTACU>2.0.CO;2.

Yan, Q., and Z. Zhang, 2017: Dominating roles of ice sheets and insolation in variation of tropical cyclone genesis potential over the North Atlantic during the last 21,000 years. *Geophys. Res. Lett.*, **44**, 10 624–10 632, https://doi.org/10.1002/2017GL075786.

——, R. Korty, and Z. Zhang, 2015: Tropical cyclone genesis factors in a simulation of the last two millennia: Results from the Community Earth System Model. *J. Climate*, **28**, 7182–7202, https://doi.org/10.1175/JCLI-D-15-0054.1.

——, T. Wei, R. Korty, J. Kossin, Z. Zhang, and H. Wang, 2016: Enhanced intensity of global tropical cyclones during the mid-Pliocene warm period. *Proc. Natl. Acad. Sci. USA*, **113**, 12 963–12 967, https://doi.org/10.1073/pnas.1608950113.

——, R. Korty, Z. Zhang, and H. Wang, 2019: Evolution of tropical cyclone genesis regions during the Cenozoic era. *Nat. Commun.*, **10**, 3076, https://doi.org/10.1038/s41467-019-11110-2.

——, ——, ——, C. Brierley, X. Li, and H. Wang, 2020: Large shift of the Pacific Walker circulation across the Cenozoic. *Natl. Sci. Rev.*, https://doi.org/10.1093/nsr/nwaa101, in press.

Yoo, J., J. Galewsky, S. J. Camargo, R. Korty, and R. Zamora, 2016: Dynamical downscaling of tropical cyclones from CCSM simulations of the Last Glacial Maximum. *J. Adv. Model. Earth Syst.*, **8**, 1229–1247, https://doi.org/10.1002/2016MS000685.

Zamora, R. A., R. L. Korty, and M. Huber, 2016: Thermal stratification in simulations of hot climates: A climatology using saturation potential vorticity. *J. Climate*, **29**, 5083–5102, https://doi.org/10.1175/JCLI-D-15-0785.1.

Zhang, L., and C. Wang, 2013: Multidecadal North Atlantic sea surface temperature and Atlantic meridional overturning circulation variability in CMIP5 historical simulations. *J. Geophys. Res. Oceans*, **118**, 5772–5791, https://doi.org/10.1002/jgrc.20390.